Volume 4
Number 17
7 September 2023
Pages 3673–3896

Materials Advances

rsc.li/materials-advances

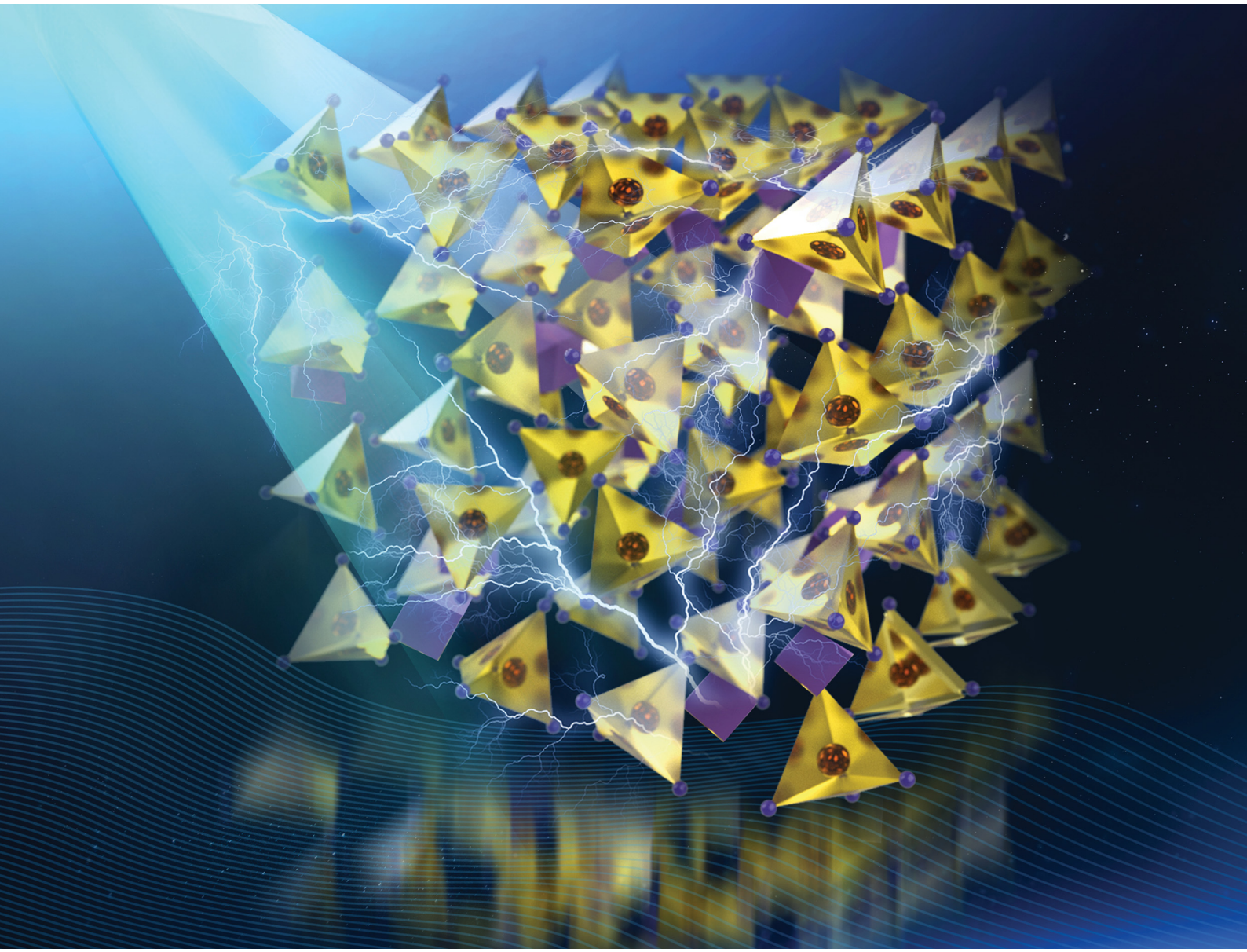

ISSN 2633-5409

ROYAL SOCIETY OF CHEMISTRY

PAPER
Lu Yao, Cai Lin Wang *et al.*
Bright lead-free $Cs_3Cu_2I_5$ perovskite scintillators for thermal neutron detection

Materials Advances

ROYAL SOCIETY OF CHEMISTRY

PAPER

View Article Online
View Journal | View Issue

Cite this: *Mater. Adv.*, 2023, 4, 3714

Bright lead-free $Cs_3Cu_2I_5$ perovskite scintillators for thermal neutron detection†

Lu Yao,* Wanting Gui, Xunsheng Zhou, Chao Li, Shi Zhang, Jing Kui Zhao and Cai Lin Wang*

Received 29th May 2023,
Accepted 15th June 2023

DOI: 10.1039/d3ma00270e

rsc.li/materials-advances

All-inorganic lead-free perovskite scintillators have attracted wide applications in X-ray imaging recently due to their low cost, high resolution, and environmental friendliness. However, their potential application in thermal neutron detection has yet to be thoroughly explored. In this article, the properties of all-inorganic perovskite $Cs_3Cu_2I_5$ scintillators for thermal neutron detection have been investigated. A simple synthesis process has been applied to produce $Cs_3Cu_2I_5$ scintillators. The as-prepared $Cs_3Cu_2I_5$ crystals exhibit intense blue emission with a photoluminescence quantum yield (PLQY) of 60.3%. A composite of ^{6}LiF, $Cs_3Cu_2I_5$, and poly(methyl methacrylate) (PMMA) has been utilized for thermal neutron detection, which has a light yield of about 28 000 photons per thermal neutron, four times that of a commercial ^{6}Li-glass (GS20) scintillator (7000 photons per thermal neutron). Effective neutron-gamma-pulse-discrimination has been achieved using a network-dynamics digital filter, effectively separating thermal neutrons from gamma events. Our composite scintillators have a high thermal neutron absorption efficiency of about 60%. In addition, $Cs_3Cu_2I_5$ crystals are more sensitive to X-ray irradiation compared to commercial Na-doped CsI scintillators. Our work provides a new strategy for large-scale perovskite-based thermal neutron detection and imaging.

1. Introduction

Thermal neutron detectors are essential components in neutron scattering, physics, the nuclear power industry, radioactive waste storage, security, nuclear medicine, and material analysis.[1–7] The most commonly used thermal neutron detectors are ^{3}He gas detectors, which exhibit a maximum detection efficiency of about 80%. However, ^{3}He gas has rarely been available in recent years and its price is increasing quickly.[8–10] Nevertheless, the need for neutron detectors is growing, especially in major science facilities such as spallation neutron sources.[11,12] As an alternative technology for ^{3}He, scintillators have great advantages. For example, the ^{6}LiF/ZnS:Ag neutron scintillator has large area coverage and high neutron detection efficiency.[13–15] However, its slow response limits the count rate capability. The self-absorption and scattering of scintillation light in the ^{6}LiF/ZnS:Ag make the scintillator opaque and limit its light output. The ^{6}Li glass (GS20) scintillator has a poor light yield and limited ability in neutron-gamma discrimination.[16,17] Other Li, Gd, and B-containing compounds, such as $Li_6Gd(BO_3)_3$ (LGBO), $Ce:Gd_3(Al,Ga)_5O_{12}$ (GAGG), $CsLiCeCl_6$, and $LiCaAlF_6$, cannot satisfy the stringent requirements of neutron detection one way or another.[18–22]

Lead-halide perovskites are promising for advanced optoelectronic devices, such as solar cells,[23] photodetectors,[24] light-emitting diodes,[25] photo-catalysts,[26] and mersisters,[27] due to their excellent photoluminescence and optoelectronic performances. However, the toxicity of lead and low stability limit their applications. All-inorganic lead-free perovskites, with outstanding photoluminescence, stability, and eco-friendliness, have attracted wide applications especially in photoluminescence devices, such as light-emitting diodes and scintillation detectors.[28,29] Copper-based halide perovskites, for example $CsCuX_3$ (X = Cl, Br, I), $RuCuX_3$, and $Cs_3Cu_2I_5$, have been researched for their high quantum efficiency, excellent photoelectric properties, and excellent stability.[30–34] Special attention has been paid to their applications in scintillators, due to their extremely high light yields, which could reach 98 200 ph per MeV (photons per MeV) for gamma detection.[35] Under X-ray radiation, copper-based perovskite scintillators exhibit high spatial resolution, excellent linear response, and low dose rate limit.[36–38] A ^{6}Li-doped $Cs_3Cu_2I_5$ single crystal has a light yield of 96 000 ph per neutron for thermal neutron radiation, which implies their potential in thermal neutron detection.[38] However, the neutron absorption efficiency of the crystal scintillator is restricted by the doping content, and the area of the scintillation screen is limited for some applications.

Neutron Science-Imaging Science and Technology, Songshan Lake Materials Laboratory, Dongguan, Guangdong 523808, China. E-mail: yaolu841118@163.com

† Electronic supplementary information (ESI) available. See DOI: https://doi.org/10.1039/d3ma00270e

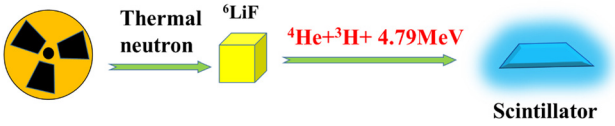

Fig. 1 Schematic of the luminescence process in a composite scintillator.

A composite scintillator would be a solution for the limited absorption efficiency and coverage. As shown in Fig. 1, under thermal neutron radiation, neutron absorbers, such as ^{6}LiF, transfer neutrons to daughter particles (α, Triton) through nuclear reactions. Then the daughter particles ionize the materials and generate secondary electrons, which dissipate their energies with phonons and thermal electrons formed. Thermal electrons will de-excite to the ground state and may generate visible light *via* electron–hole recombination. The neutron absorption efficiency can be adjusted by the loading fraction of absorption material in the composite scintillators.

In this work, we have fabricated copper based all-inorganic, lead-free perovskite scintillators for thermal neutron detection with high absorption efficiency and light yield. A composite of ^{6}LiF, $Cs_3Cu_2I_5$, and poly(methyl methacrylate) (PMMA) has been developed, which has a light yield of about 28 000 ph per thermal neutron, 4 times that of the commercial standard neutron GS20 scintillator. The thermal neutron absorption efficiencies are about 60%, much higher than those of Li-doped $Cs_3Cu_2I_5$ crystals. This work provides a new scintillator with high efficiency and large coverage for thermal neutron detection and imaging.

2. Methods

2.1 Chemicals

All reagents were used without further purification, unless otherwise stated. Cesium iodide (CsI, 99.9%), copper iodide (CuI, 99.9%), dimethyl formamide (DMF, 99.9%), tween 80 ($C_{24}H_{44}O_6$, Medical grade), and hypophoaphoeous acid (50%) were the original reagents purchased from Aladdin Corporation. ^{6}LiF powders were originally from Eljen Technology (TX, USA), and polymethyl methacrylate (PMMA) powders were from Nanjing DuLai Biotechnology Corporation, China.

2.2 Preparation

Synthesis of $Cs_3Cu_2I_5$ crystals. CuI (0.3038 g), CsI (0.6238 g), 80 μL of Tween80 and 80 μL of hypophoaphoeous were dissolved in 4 mL of DMF with ultrasonication for 1 minute. The mixed solution became transparent immediately, and then it was poured into a Petri dish, and left in a fume hood. After being volatilized for several days, strip-shape crystals were obtained. The synthetic volume can be directly scaled up to produce large quantity crystal powders.

Preparing $Cs_3Cu_2I_5$/^{6}LiF/PMMA composite films. First, ^{6}LiF and PMMA powders with a weight ratio of 1 : 2 were mixed. Then, different amounts of $Cs_3Cu_2I_5$ were added to the mixed powders and ground for several minutes. The weight ratio of the $Cs_3Cu_2I_5$ to ^{6}LiF powders was 0.1 : 1, 0.3 : 1, 0.5 : 1, 1 : 1, and 1.5 : 1 for making five samples, respectively. The mixed powders were dissolved in dichloromethane, sonicated for a few seconds, and poured into a mold with a diameter of 25 mm and thickness of 0.5 mm, and transparent plastic composite scintillators were obtained. A schematic of the preparation process is shown in Fig. S1 (ESI†).

Preparing $Cs_3Cu_2I_5$/Gd_2O_3/PMMA composite films. The $Cs_3Cu_2I_5$/Gd_2O_3/PMMA composite films are prepared using the same procedure as $Cs_3Cu_2I_5$/^{6}LiF/PMMA composite films, with the weight ratio 1 : 0.1 : 2.

2.3 Characterization

The structural characterization of the $Cs_3Cu_2I_5$ crystal powders was carried out on an X-Ray Diffractometer (Rigaku, Miniflex 600; CuKα radiation, 40 kV, 15 mA), with measurements taken from 2θ of 10°–60°. The morphological characterization was conducted using an optical microscope. Photoluminescence (PL) and photoluminescence excitation (PLE) spectra were recorded with a photoluminescence spectrometer (Zolix, Omnifluo 900) equipped with a cryostat. An X-ray tube (Tungsten target, 30–200 keV) was also used as the source and combined with the spectrometer for radio-luminescence (RL) measurements. Optical transmission spectra were performed using a HATACHI UH4150 UV-Vis-NIR-absorption spectrometer. The pulse-height spectra were measured by a home-built system, which included a photomultiplier tube (PMT, ET Enterprises, 9124B), a pre-amplifier (Ortec, 9305), a shaping amplifier (Ortec, 572A, 3 μs shaping time), and a multichannel analyzer (MCA, Ortec, Eesy-MCA-8k). Scintillation decay time was measured using an oscilloscope (Agilent, MSO9254A). The measurement details can be found in our previous report.[18] Thermal neutron radiation was obtained from ^{252}Cf (average energy = 25 meV, emission rate = 2000 n s^{-1}) with a polythylene (thickness = 500 mm) moderated cavity. Gamma radiation was obtained from ^{60}Co (average energy = 1.2 MeV) and ^{137}Cs (energy = 0.662 MeV).

3. Results and discussion

The strip-shape $Cs_3Cu_2I_5$ crystals obtained from the evaporative crystallization have a length of 2–3 mm (Fig. 2b). In Fig. 2c, the XRD patterns show that the main product is $Cs_3Cu_2I_5$ (PDF# 45-0077) with a *Pbnm* (62) space group, and the impurity phase is $CsCu_2I_3$ (PDF# 01-077-0069). As shown in Fig. 2a, the crystal structure of $Cs_3Cu_2I_5$ has edge-sharing $[Cu_2I_3]^-$ anionic chains separated by rows of Cs^+ atoms. Two different types of Cu^+ exist, one is located at the center of the tetrahedral gap, while the other is situated in the center of the triangle.[39] In this crystal structure, the exciton is confined by the structural barrier inside the crystal lattice, exhibiting a 0D structure, which modifies the electronic bands into discrete energy levels and enhances the photoluminescence of the material.[40] The optical characteristics are shown in Fig. 2(d), and the PLE and PL peaks are located at 320 and 440 nm, respectively. There is a large Stokes shift of 120 nm (1.06 eV), which can be considered as a feature of self-trapped exciton (STE) emission formed by strong electron–phonon coupling. There is no overlap between excitation and emission peaks, implying no self-absorption, which is favorable for RL. The optical property of

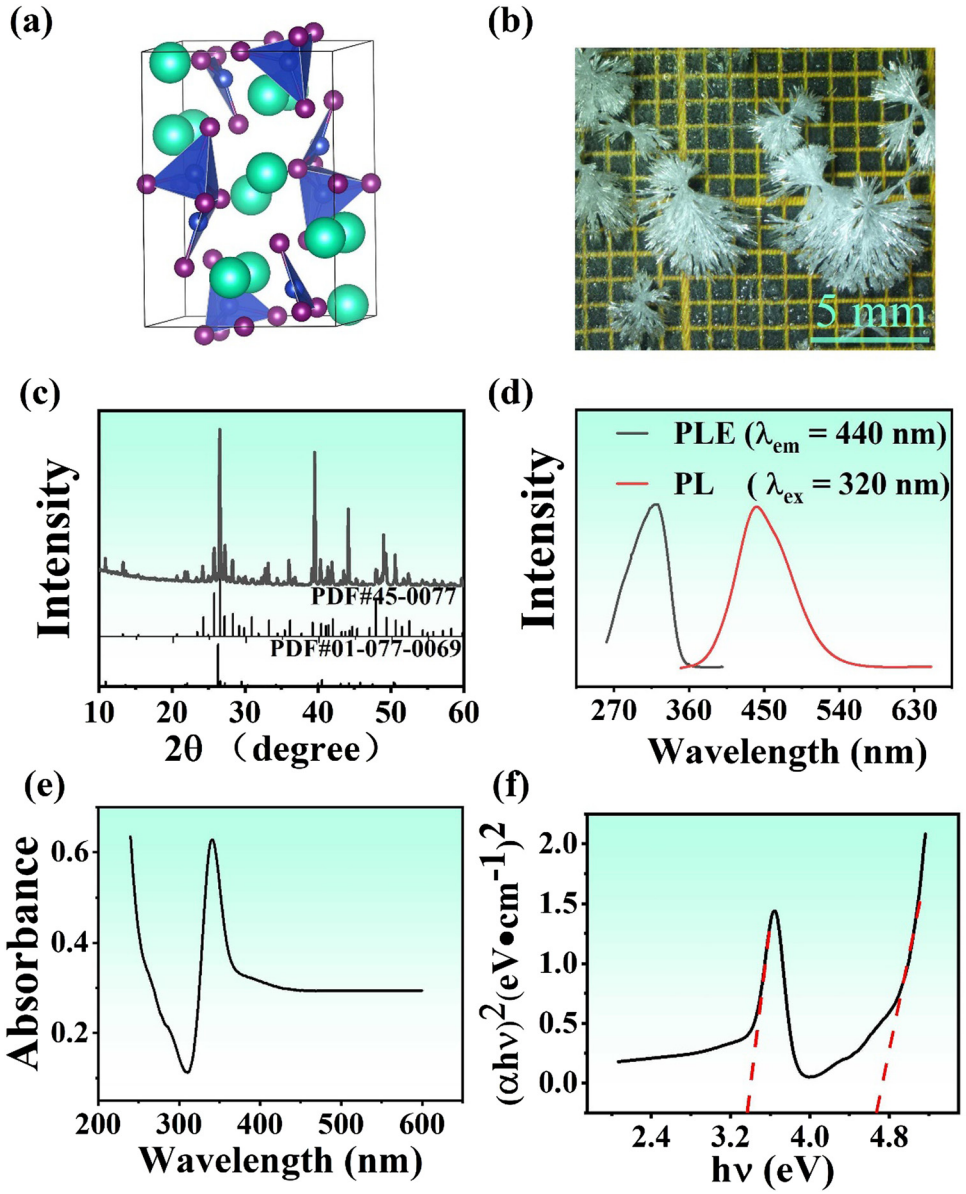

Fig. 2 Structural and optical characteristics of $Cs_3Cu_2I_5$ crystals: (a) crystal structure (green balls refer to Cs atoms, purple balls refer to I atoms, blue balls refer to Cu atoms), (b) microphotograph, (c) X-ray diffraction patterns, (d) PL emission (λ_{ex} = 320 nm) and excitation (λ_{em} = 440 nm) spectra, (e) absorption spectra, and (f) the $(\alpha h\nu)^2$ *versus* $h\nu$ plots.

the impurity phase has also been examined (Fig. S2, ESI†), with a PL excitation peak and an additional weak PL emission peak of the $CsCu_2I_3$ located at 333 and 550 nm, respectively. Compared with $Cs_3Cu_2I_5$, $CsCu_2I_3$ shows much weaker absorbance and emission. To examine the photoluminescence quantum yield (PLQY) of the as-prepared $Cs_3Cu_2I_5$ crystals, an absolute photoluminescence measurement with an integrating sphere was conducted and a PLQY of 60.3% was obtained (Fig. S3, ESI†). Based on DFT calculation, $Cs_3Cu_2I_5$ has a direct band gap.[41] The absorption spectra were measured (Fig. 2e), and the optical band gap (E_g) of $Cs_3Cu_2I_5$ was calculated by the classical Tauc formula.

$$\alpha h\nu = A\left(h\nu - E_g\right)^{\frac{1}{2}} \quad (1)$$

where A, h, ν, and α are a constant, the Planck constant, light frequency, and absorption coefficient, respectively. E_g is estimated to be 4.6 eV, which further confirmed the UV absorption, implying potential ability of scintillation. A band edge absorption belonging to $CsCu_2I_3$ has also been observed, which is estimated to be 3.83 eV (Fig. 2f), consistent with the previous reports.[42]

To test the RL properties of the crystal, the RL intensity of $Cs_3Cu_2I_5$ to the X-ray dose rate has been measured (Fig. S4, ESI†). One emission peak located around 440 nm is observed from $Cs_3Cu_2I_5$ but not from $CsCu_2I_3$. Therefore, the impurity phase has no impact on the RL performance. The linear relationship between scintillation light intensity and X-ray dose rate is crucial for its application in X-ray imaging. The integration intensity of the spectra shows a linear relationship with the

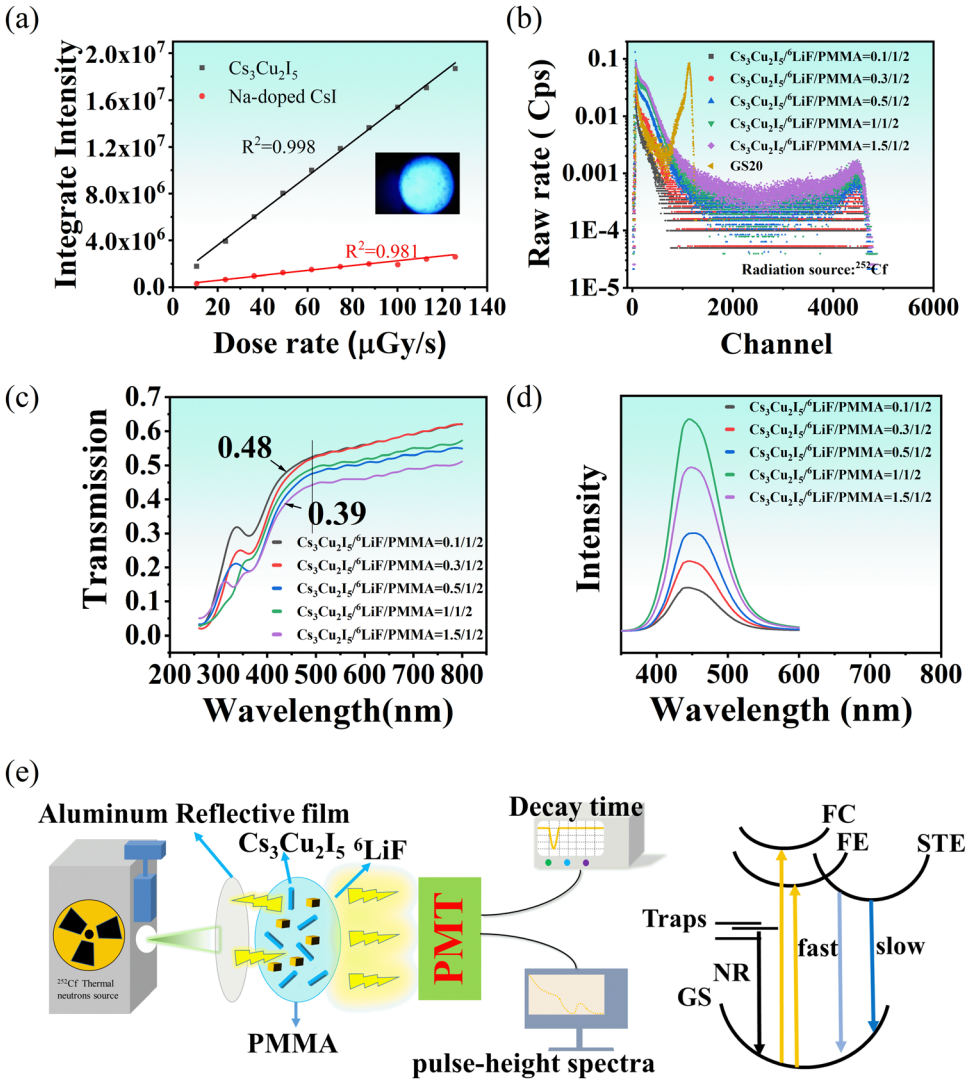

Fig. 3 RL properties of $Cs_3Cu_2I_5$ and the as-prepared composites: (a) RL intensity *versus* X-ray dose rate of the crystals in comparison with Na-doped CsI, the inset photo is the RL luminescence photograph of the $Cs_3Cu_2I_5$ crystals, (b) pulse height spectra under thermal neutron radiation, (c) transmission spectra, (d) RL spectra excited by the X-ray tube of the composite films with different amounts of $Cs_3Cu_2I_5$ crystals, (e) schematics of neutron detection and RL dynamics of the neutron scintillators. FC refers to free carriers, FE refers to free excitons, GS refers to ground state, NR refers to non-radiative process.

dose rate in the range of 10 μGy s^{-1} to 125 μGy s^{-1} (Fig. 3a). In comparison, the RL intensities of Na-doped CsI powders irradiated by different X-ray dose rates under the same conditions were demonstrated. The X-ray dose rate *versus* RL intensity was found to be linear ($y = kx + b$). The slope k of the linear fitting can be used as the sensitivity factor to X-rays; the larger the slope, the more sensitive to X-rays. The sensitivity factor of the as-prepared $Cs_3Cu_2I_5$ crystals ($k = 1.47 \times 10^5$) is almost one order of magnitude higher than that of Na-doped CsI powders ($k = 1.89 \times 10^4$). Hence, the as-prepared $Cs_3Cu_2I_5$ crystals may replace the commercial Na-doped CsI as an X-ray dosimeter.

For neutron scintillators, the match between their emission wavelength and PMT sensitivity band is essential. In our experiment, the sensitivity band of a typical PMT is between 300 and 500 nm, and the quantum efficiency between 350 and 450 nm is higher than 25%. Therefore, a scintillator emitting light between 350 and 450 nm would be better. Intense blue emission has been detected under X-ray excitation with an emission peak at 448 nm (Fig. 3d), which matches perfectly with the PMT. In addition, neutron absorption elements such as ^{6}Li and Gd are prerequisites for neutron detection. However, $Cs_3Cu_2I_5$ lacks these elements, so $Cs_3Cu_2I_5$/^{6}LiF/PMMA and $Cs_3Cu_2I_5/Gd_2O_3$/PMMA composite films were prepared. Under thermal neutron radiation, nuclear reactions occur in ^{6}Li and Gd. $Cs_3Cu_2I_5$ absorbs high energy photons released in nuclear reaction through a photoelectric effect, which generates massive electron–hole pairs. The energetic charge carriers are thermalized, and then thermalized electrons accumulate at the conduction band, as do the holes at the valence band, leading to the formation of free excitons. The free excitons become self-trapped by the structure distortions that are caused by the excitation of electrons. At the end of the process, the

self-trapped excitons annihilate through photon emission *via* fast and slow decay processes. At the same time, the thermal electrons may be captured by defects and decay in a non-radiative process. The emitted photons are collected by a PMT, whose output signals are read by the pulse height spectrometer and Oscilloscope (Fig. 3e).

The $Cs_3Cu_2I_5/Gd_2O_3$/PMMA composite has much lower light yields than the $Cs_3Cu_2I_5/^6$LiF/PMMA (Fig. S6, ESI†), even though it has comparable absorption efficiency (Fig. S5, ESI†). The detailed discussions are presented in the ESI.† The pulse height spectra show that $Cs_3Cu_2I_5/^6$LiF/PMMA films have a high light yield, which is about four times that of the commercial GS20 scintillator (Fig. 3b). The peak channel numbers of the GS20 and $Cs_3Cu_2I_5/^6$LiF/PMMA films are 1129 and 4485. Considering commercial GS20 with a light yield of about 7000 photons per thermal neutron as a reference, the light yield of $Cs_3Cu_2I_5/^6$LiF/PMMA films is 28 000 photons per thermal neutron. However, the raw count rate of thermal neutrons from $Cs_3Cu_2I_5/^6$LiF/PMMA films is lower than that of the commercial GS20, probably due to its lower light transmission. Count rates or neutron efficiency is critical for scintillators and needs more careful optimization in our future work. To optimize the ratio of $Cs_3Cu_2I_5$ to ^{6}LiF for higher detection efficiency, different amounts of $Cs_3Cu_2I_5$ crystals were added to the composite films. The raw rates of the $Cs_3Cu_2I_5/^6$LiF/PMMA films first increase with the increasing ratio of $Cs_3Cu_2I_5$ crystals, and then remain the same with further increase of the $Cs_3Cu_2I_5$ crystals (Fig. 3b). The peak channel number, which is the indicator for light yield, stays stable for all five $Cs_3Cu_2I_5/^6$LiF/PMMA films. In the scintillator, the light yield can be expressed by N_{ph}, the number of UV/visible photons produced per energy E of incoming radiation photons, which can be calculated by the following eqn (2).[43]

$$N_{ph} = \left\{\frac{E}{\beta E_g}\right\} SQ \quad (2)$$

where E_g is the band gap of the material, and S and Q represent the quantum efficiency of the transport and luminescence stages, respectively. β is the phenomenological parameter, which is in a range of 2–3 in most materials. Therefore, N_{ph} is decided by E_g. In $Cs_3Cu_2I_5/^6$LiF/PMMA films, E_g is the same from one sample to the other, so the light yield remains the same in all five samples. Enhancing the $Cs_3Cu_2I_5$ loading fraction can only increase the raw count rates. With increasing ratio of $Cs_3Cu_2I_5$ loading fraction, more energy absorbed by ^{6}LiF can be transferred to $Cs_3Cu_2I_5$. However, as the loading fraction of $Cs_3Cu_2I_5$ continues to increase, the light transmission efficiency decreases due to the refractive index difference between the matrix and the particles and the increased scattering of light by the particles. When the $Cs_3Cu_2I_5$ weight ratio increased from 0.1 to 1.5, the light transmission decreased from 0.48 to 0.39 (Fig. 3c). Therefore, we conclude that $Cs_3Cu_2I_5/^6$LiF/PMMA with a weight ratio of 1/1/2 has the best RL performance in our experiments. To characterize the structure and morphology of the composite films. The XRD pattern and SEM image of the as-prepared composite films with a weight ratio for 1/1/2 were measured (Fig. S7, ESI†). In Fig. S7a (ESI†), the orthorhombic phase of $Cs_3Cu_2I_5$ (PDF# 45-0077) and cubic phase of LiF (PDF# 001-1270) are identified. The phase of $Cs_3Cu_2I_5$ in the composite material is the same as that in the crystal, implying that the mixing process has no effect on the structure of $Cs_3Cu_2I_5$. In Fig. S7b and c (ESI†), the mixed $Cs_3Cu_2I_5$ and ^{6}LiF assembled together with a sphere-like shape, and dispersed in the PMMA substrates. The $Cs_3Cu_2I_5$ crystals are ground to a micro-sheet shape, whereas ^{6}LiF powders keep a cubic shape. The thickness of the composite films is the same as the mold depth, which is about 0.5 mm (Fig. S8, ESI†).

To further verify the above results, the RL intensity spectra under X-ray excitation of the as-prepared $Cs_3Cu_2I_5/^6$LiF/PMMA films with different amounts of $Cs_3Cu_2I_5$ powder (Fig. 3d) were measured, which shows the same tendency. The RL intensity initially increases with the growing amount of $Cs_3Cu_2I_5$ powder. With further increasing amounts of the $Cs_3Cu_2I_5$ crystals, the RL intensity starts to decrease due to the decreased transmission rates of the as-prepared $Cs_3Cu_2I_5/^6$LiF/PMMA films, which can also be identified from the transmission spectra (Fig. 3c).

From the point of view of statistics, the neutron-gamma discrimination (NGD) ratio is crucial for the practical application of thermal neutron scintillators, especially for efficient neutron detectors with high signal-to-noise ratios.[44] To estimate the neutron-gamma discrimination capability and count rate capability, the decay curves of scintillators under different radiation sources were collected (Fig. 4a). They can be fitted by two exponential decay functions:

$$I(t) = A_1 \exp\left(-\frac{t}{\tau_{fast}}\right) + A_2 \exp\left(\frac{t}{\tau_{slow}}\right) \quad (3)$$

where, $I(t)$ is the time-dependent scintillation light intensity; A_1 and A_2 are the fitting parameters; τ_{fast} and τ_{slow} are the fast and slow lifetimes. The fitting results and average decay lifetime τ_{Avg} are listed in Table 1. The fast components might come from the defects in the surface, which may have higher concentrations than those in the inner crystal. The slow components might arise from localized excitons. $Cs_3Cu_2I_5$ is a typical 0D structure perovskite, the isolated copper centers $[Cu_2I_5]^{3-}$ separated by Cs^+ ions lead to localized excitons, which result in slow electron–hole recombination. The average decay lifetime of the $Cs_3Cu_2I_5$ under a ^{252}Cf neutron source is 359 ns. The figure of merit (FoM) value of $Cs_3Cu_2I_5$ is defined as the ratio of light yield to average decay lifetime.[45] The FoM calculated for the composite films is higher in comparison with several representative scintillators (Fig. 4b and Table S3, ESI†), except for GS20 and LiI:Eu.

As indicated in Table 1 and Fig. 4a, the decay dynamic processes of neutron and gamma are different, which would influence the NGD capability. The NGD using pulse shape difference was conducted using a conventional two-feature S_1–S_2 plot,[44,46] which has been used in our previous reports. S_1 and S_2 are the integration values of individuals pulsed in the lifetime windows of [−50,0] ns and [0,50] ns, respectively. As shown in Fig. 4c, a two-dimensional scatter plot of S_1–S_2 can separate most of the neutron events from the gammas using the blue solid line as the class boundary. The boundary is set to

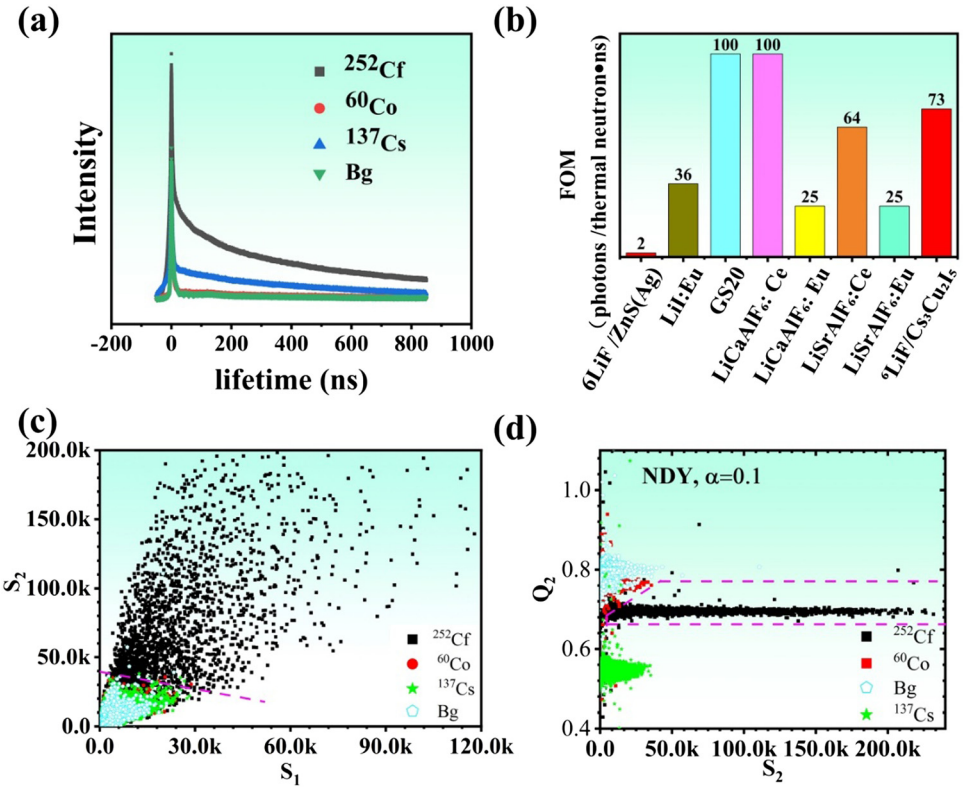

Fig. 4 RL properties of the composite ($Cs_3Cu_2I_5$/^{6}LiF/PMMA = 1 : 1 : 2): (a) decay curves under the irradiation of ^{60}Co, ^{252}Cf and ^{137}Cs and backgrounds, (b) the FoM in comparison with several well-known neutron scintillators. Neutron-gamma discrimination (NGD) films calculated by two methods, (c) conventional two-feature S_1–S_2 plot and (d) gamma-embedded non-negative matrix factorization (GNMF) method. In (d) Q_2 is the second vector of projected matrix $Q_2 = H(L)V$, $H = 1/(1 + \alpha L)$ is the network dynamics filter, L is the Laplacian operator of the event graph, α is a hyperparameter, and V is the signal matrix.[44]

Table 1 Scintillation decay lifetime components under thermal neutron radioactive sources of $Cs_3Cu_2I_5$/^{6}LiF/PMMA films

Radiation sources	τ_{fast} (ns)	τ_{slow} (ns)	τ_{Avg} (ns)
^{60}Co	5.4 (67%)	261 (33%)	250
^{137}Cs	4.0 (95%)	330 (5%)	270
^{252}Cf	3.9 (79%)	373 (21%)	359

obtain both a neutron efficiency and an NGD ratio as high as possible. Events above and below this line are assigned to neutrons and gamma-rays, respectively. From the above boundary, the thermal neutron efficiency is calculated to be 22% (relative to a GS20 detector) and the NGD ratio is 8×10^4. The values of NGD ratio and neutron detection efficiency provided by the S_1–S_2 plot are not good enough for practical applications of neutron detection. Therefore, a graph-embedded network dynamic digital filter (NYD) method for discrimination is applied to improve both the neutron detection efficiency and NGD ratio, and the results are shown in Fig. 4d. In this method, an event graph (or network) is established to describe the data measured under ^{252}Cf, ^{137}Cs and ^{60}Co sources and background. A batch of unlabeled events is regarded as graph signals, whose low-dimensional representations are searched under the assumption of smoothness in the high-dimensional event graph. The detailed description of the method can be found in our previous reports.[44,46] As shown in Fig. 4d, a boundary composed of three lines can separate neutron and gamma. There is an almost clean separation between neutron and background events. A thermal neutron detection efficiency of 43% (relative to a GS20 detector) and an NGD ratio of about 2×10^5 are obtained, which are much better than those obtained by the traditional S_1–S_2 method.

To gain more insight into the STE dynamics and electron–phonon interaction, temperature-dependent photoluminescence excited (PLE) spectra at 444 nm (Fig. 5a) and emission spectra under 292 nm excitation (Fig. 5b inset) were measured. The PLE spectra exhibit red shifts with increasing temperature, which implies a decrease in the energy gap. This phenomenon has also been found in other materials such as carbon quantum dots and PbS,[47–49] which can be explained by

$$E_g T = E_{g0} - \alpha \frac{T^2}{(T + \beta)} \quad (4)$$

where E_{g0} is the energy gap at 0 K, α is the temperature coefficient, and the value of β is close to the Debye temperature of the material. From eqn (4), the temperature elevation leads to a decrease of the energy gap, resulting in red shifts of the PLE spectra. Three excitation peaks were detected at cryogenic temperature (Fig. 5d). A fit to a sum of three Gaussians provides peak positions at 3.84 eV, 4.26 eV and 4.54 eV. The peak position at 3.84 eV is assigned to tiny impurities of $CsCuI_3$ in

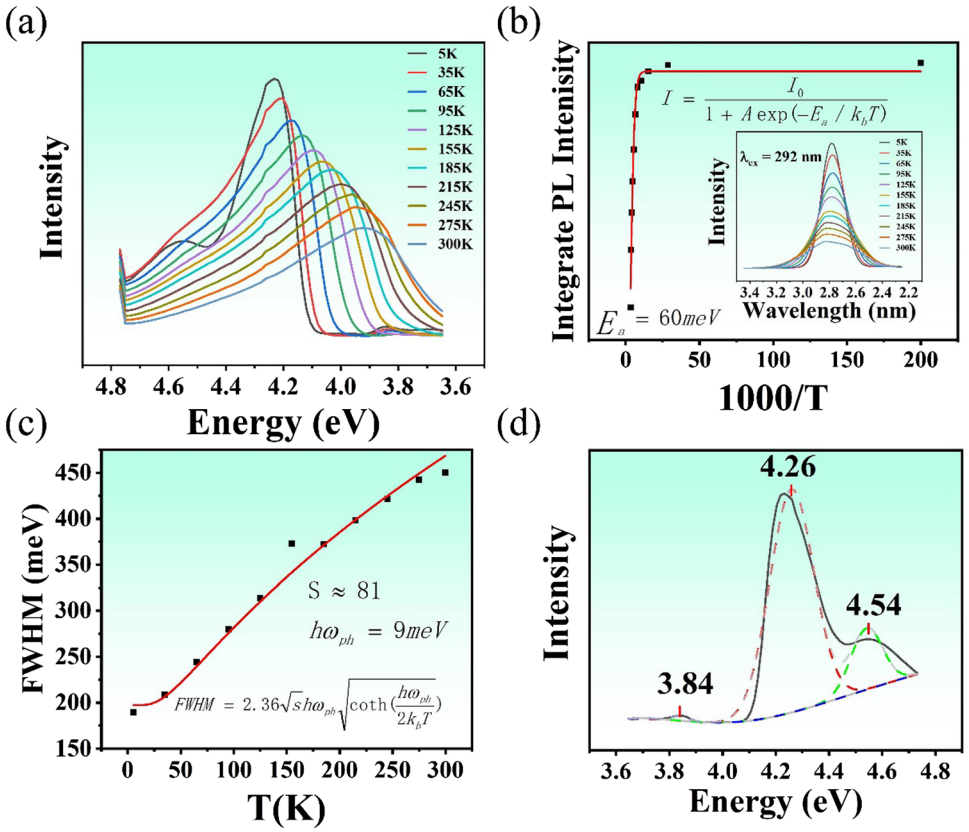

Fig. 5 Temperature dependences of photoluminescence properties of the as-prepared $Cs_3Cu_2I_5$ crystals, (a) photoluminescence excited spectra at 444 nm; (b) integrated PL intensities of the emission spectra under 292 nm excitation from 5 K to 300 K, the inset is the emission spectra; (c) FWHMs of the emission peak; (d) photoluminescence excited spectrum at 5 K.

the products, which are reported by Chen *et al.*[50] The peak positions at 4.26 eV and 4.54 eV result from the excitonic absorption peak and band edge absorption peak, respectively.[51] Usually, the band edge absorption peak cannot be identified in PLE spectra. However, with the temperature decreased to cryogenic temperature, we can clearly see the split of the band edge absorption and excitonic absorption.

Temperature-dependent PL measurements are effective to obtain the photoluminescence properties, including activation energy, the Huang–Rhys factor and phonon frequency. The temperature dependent PL spectra were measured and the results show an obvious spectral quenching and broadening (Fig. 5b inset). Temperature-dependent integrated intensity can be fitted by the Arrhenius equation:

$$I(T) = \frac{I_0}{1 + c\exp\left(-\frac{E_a}{k_b T}\right)} \quad (5)$$

where $I(T)$ and I_0 are the integrated PL intensities at temperature T and the initial temperature (4 K), respectively; C is a constant; E_a is activation energy and k_b is the Boltzmann constant. The E_a is evaluated to be 57 meV (Fig. 5b), which is much lower than the previously reported values of about 130 to 400 meV.[52–54] This may arise from different thermal activating processes. Wang and Lin assumed that the thermal dissociation process originated from the excitons' annihilation at higher temperatures.[52,54] Therefore, E_a can be considered as the binding energy of excitons. However, there are other processes that might affect the thermal quenching. For example, the STE might be thermally activated to the cross point of the VB state and STE state, and back to the ground state through a non-radiative process.

The PL broadening *versus* temperature implies that electrons are distributed to more self-trapped energy states. The temperature-dependent full-width-at-half-maximum (FWHM) of PL is plotted in Fig. 5c. The Huang–Rhys factor (S), which reflects the strength of electron–phonon coupling, is obtained by fitting the temperature dependent FWHM of the emission peaks using the following equation:

$$\mathrm{FWHM} = 2.36\sqrt{S}h\omega_{\mathrm{phonon}}\sqrt{\coth\left(\frac{hw_{\mathrm{phonon}}}{2k_b T}\right)} \quad (6)$$

where $h\omega_{\mathrm{phonon}}$ is the phonon frequency. S and $h\omega_{\mathrm{phonon}}$ are calculated as 81 and 9 meV, respectively. The Huang–Rhys factor is higher than that of conventional emitters such as CdSe, ZnSe and $CsPbBr_3$ $Cs_3Sb_2I_9$, $Cs_3Bi_2I_9$ $Rb_3Sb_2I_9$ perovskites, indicating the easy formation of STEs in $Cs_3Cu_2I_5$ (Table S4, ESI†).

4. Conclusion

Our optimized composite scintillator ($Cs_3Cu_2I_5$/^{6}LiF/PMMA = 1 : 1 : 2) has a light yield of about 28 000 photons per thermal neutron, four times that of the commercial GS20 scintillator. In addition, it has excellent neutron-gamma discrimination capability (NGD ratio = 2×10^5) and the FoM is higher than those of most commercial neutron scintillators. Its thermal neutron absorption efficiency is about 60%. Although the neutron induced average decay lifetime is a little long (352 ns), doping engineering would reduce it, which will be studied in the future. This composite scintillator provides a new avenue for large-scale thermal neutron detection and imaging, and may find wide applications in the neutron scattering, homeland security, industrial nondestructive testing, and nuclear medicine.

Conflicts of interest

There are no conflicts to declare.

Acknowledgements

This work was supported by the Key-Area Research and Development Program of Guangdong Province, China (no. 2020B0303090001), Key Basic and Applied Research of Guangdong-Dongguan Joint Program (no. 22S603N111), Guangdong Basic and Applied Basic Research Foundation (no. 2021B1515120040), National Natural Science Foundation of China Major Instrument Project (no. 52127817), and Guangdong Basic and Applied Basic Research Foundation (no. 22S7061N111).

References

1 R. T. Kouzes, E. R. Siciliano, J. H. Ely, P. E. Keller and R. J. McConn, Passive neutron detection for interdiction of nuclear material at borders, *Nucl. Instrum. Methods Phys. Res., Sect. A*, 2008, **584**(2), 383–400.
2 S. M. Carturan, T. Marchi, E. Fanchini, R. De Vita, P. Finocchiaro and A. Pappalardo, Scintillator and solid-state neutron detectors and their applications, *Eur. Phys. J. Plus*, 2014, **129**(10), 212.
3 M. V. Trenikhin, *et al.*, International Multidisciplinary Microscopy Congress, *Springer Proc. Phys.*, 2014, **154**, 159.
4 Z. W. Bell, M. A. Miller, L. Maya, G. M. Brown and F. V. Sloop, Boron-loaded silicone rubber scintillators, *IEEE Trans. Nucl. Sci.*, 2004, **51**(4), 1773–1776.
5 D. M. Duxbury, N. J. Rhodes, E. M. Schooneveld, E. J. Spill and J. R. P. Webster, SPRINTER: A New Detector System for the INTER Neutron Reflectometer, *IEEE Trans. Nucl. Sci.*, 2013, **60**(2), 1327–1331.
6 R. T. Kouzes, E. R. Siciliano, J. H. Ely, P. E. Keller and R. J. McConn, Passive neutron detection at borders, 2007 IEEE Nuclear Science Symposium Conference Record, 2007, pp. 1115–1119.
7 L. Ovechkina, K. Riley, S. Miller, Z. Bell and V. Nagarkar, Gadolinium loaded plastic scintillators for high efficiency neutron detection, *Phys. Procedia*, 2009, **2**(2), 161–170.
8 R. T. Kouzes, A. T. Lintereur and E. R. Siciliano, Progress in alternative neutron detection to address the helium-3 shortage, *Nucl. Instrum. Methods Phys. Res., Sect. A*, 2015, **784**, 172–175.
9 L. J. Wittenberg, E. N. Cameron, G. L. Kulcinski, S. H. Ott, J. F. Santarius, G. I. Sviatoslavsky, I. N. Sviatoslavsky and H. E. Thompson, A Review of 3He Resources and Acquisition for Use as Fusion Fuel, *Fusion Technol.*, 1992, **21**(4), 2230–2253.
10 A. J. Hurd and R. T. Kouzes, Why new neutron detector materials must replace helium-3, *Eur. Phys. J. Plus*, 2014, **129**(10), 236.
11 R. G. Cooper, SNS detector plans, *Nucl. Instrum. Methods Phys. Res., Sect. A*, 2004, **529**(1), 394–398.
12 D. Kramer, For some, helium-3 supply picture is brightening, *Phys. Today*, 2011, **64**(5), 20–22.
13 F. Pino, L. Stevanato, D. Cester, G. Nebbia, L. Sajo-Bohus and G. Viesti, Study of the thermal neutron detector ZnS(Ag)/LiF response using digital pulse processing, *J. Instrum.*, 2015, **10**(08), T08005.
14 C. Wu, B. Tang, Z. J. Sun, Q. Zhang, Z. Yang, J. Zhang, Y. D. Yang, J. C. Liang and J. J. Wu, A study of ZnS(Ag)/6LiF with different mass ratios, *Radiat. Meas.*, 2013, **58**, 128–132.
15 C. L. Wang, M. L. Crow, L. L. Funk, B. W. Hannan, J. P. Hodges and R. A. Riedel, Optimizing ZnS/6LiF scintillators for wavelength-shifting-fiber neutron detectors, 2015 IEEE Nuclear Science Symposium and Medical Imaging Conference (NSS/MIC), 2015, pp. 1–6.
16 R. Engels, U. Clemens, G. Kemmerling, H. Nöldgen and J. Schelten, Position-sensitive detectors of the detector group at Jülich, *Nucl. Instrum. Methods Phys. Res., Sect. A*, 2009, **604**(1), 147–149.
17 R. Kurz, K. D. Muller, J. Schelten, A. Szepesvary, W. Schafer and G. Will, High resolution position-sensitive detector for thermal neutrons, *IEEE Trans. Nucl. Sci.*, 1988, **35**(1), 78–80.
18 X. Zhou, C. L. Wang and Y. Wang, Transparent Microcomposite Films Based on a Ce-Doped $Li_6Gd(BO_3)_3$ Scintillator for Radiation Detection, *ACS Omega*, 2022, **7**(35), 31567–31576.
19 J. B. Czirr and T. K. McKnight, An improved detector for powder diffractometers, *Nucl. Instrum. Methods Phys. Res., Sect. A*, 2004, **529**(1), 268–273.
20 P. A. Rodnyi, V. B. Mikhailik, G. B. Stryganyuk, A. S. Voloshinovskii, C. W. E. van Eijk and G. F. Zimmerer, Luminescence properties of Ce-doped Cs2LiLaCl6 crystals, *J. Lumin.*, 2000, **86**(2), 161–166.
21 M. Flaska, S. A. Pozzi and J. B. Czirr, Use of an LGB detector in nuclear nonproliferation applications, *2008 IEEE Nuclear Science Symposium Conference Record*, 2008, pp. 3376–3380.
22 C. W. Ev Eijk, J. T. Md Haas, P. Dorenbos, K. W. Kramer and H. U. Gudel, Development of elpasolite and monoclinic thermal neutron scintillators, IEEE Nuclear Science Symposium Conference Record 2005, 2005, pp. 239–243.
23 S. Sahare, H. D. Pham, D. Angmo, P. Ghoderao, J. MacLeod, S. B. Khan, S.-L. Lee, S. P. Singh and P. Sonar, Emerging Perovskite Solar Cell Technology: Remedial Actions for the Foremost Challenges, Advanced Energy, *Materials*, 2021, **11**(42), 2101085.

24 L. Li, S. Ye, J. Qu, F. Zhou, J. Song and G. Shen, Recent Advances in Perovskite Photodetectors for Image Sensing, *Small*, 2021, **17**(18), 2005606.
25 Q. Van, Le, H. W. Jang and S. Y. Kim, Recent Advances toward High-Efficiency Halide Perovskite Light-Emitting Diodes: Review and Perspective, Small, *Methods*, 2018, **2**(10), 1700419.
26 K. S. Schanze, P. V. Kamat, P. Yang and J. Bisquert, Progress in Perovskite Photocatalysis, *ACS Energy Lett.*, 2020, **5**(8), 2602–2604.
27 X. Xiao, J. Hu, S. Tang, K. Yan, B. Gao, H. Chen and D. Zou, Recent Advances in Halide Perovskite Memristors: Materials, Structures, Mechanisms, and Applications, *Adv. Mater. Technol.*, 2020, **5**(6), 1900914.
28 Y. Zhang, Y. Ma, Y. Wang, X. Zhang, C. Zuo, L. Shen and L. Ding, Lead-Free Perovskite Photodetectors: Progress, Challenges, and Opportunities, *Adv. Mater.*, 2021, **33**(26), 2006691.
29 Y. Tang, S. Tang, M. Luo, Y. Guo, Y. Zheng, Y. Lou and Y. Zhao, All-inorganic lead-free metal halide perovskite quantum dots: progress and prospects, *Chem. Commun.*, 2021, **57**(61), 7465–7479.
30 R. Roccanova, A. Yangui, G. Seo, T. D. Creason, Y. Wu, D. Y. Kim, M.-H. Du and B. Saparov, Bright Luminescence from Nontoxic $CsCu_2X_3$ (X = Cl, Br, I), ACS, *Mater. Lett.*, 2019, **1**(4), 459–465.
31 X. Xu, C. Fan, Z. Qi, S. Jiang, Q. Xiao, H. Liang, H. Duan and Q. Zhang, CsCu2I3 Nanoribbons on Various Substrates for UV Photodetectors, *ACS Appl. Nano Mater.*, 2021, **4**(9), 9625–9634.
32 X. Mo, T. Li, F. Huang, Z. Li, Y. Zhou, T. Lin, Y. Ouyang, X. Tao and C. Pan, Highly-efficient all-inorganic lead-free 1D $CsCu_2I_3$ single crystal for white-light emitting diodes and UV photodetection, *Nano Energy*, 2021, **81**, 105570.
33 M. Zhang, J. Zhu, B. Yang, G. Niu, H. Wu, X. Zhao, L. Yin, T. Jin, X. Liang and J. Tang, Oriented-Structured CsCu2I3 Film by Close-Space Sublimation and Nanoscale Seed Screening for High-Resolution X-ray Imaging, *Nano Lett.*, 2021, **21**(3), 1392–1399.
34 B. Yang, L. Yin, G. Niu, J.-H. Yuan, K.-H. Xue, Z. Tan, X.-S. Miao, M. Niu, X. Du, H. Song, E. Lifshitz and J. Tang, Lead-Free Halide Rb_2CuBr_3 as Sensitive X-Ray Scintillator, *Adv. Mater.*, 2019, **31**(44), 1904711.
35 L. Stand, D. Rutstrom, M. Koschan, M.-H. Du, C. Melcher, U. Shirwadkar, J. Glodo, E. Van Loef, K. Shah and M. Zhuravleva, Crystal growth and scintillation properties of pure and Tl-doped $Cs_3Cu_2I_5$, *Nucl. Instrum. Methods Phys. Res., Sect. A*, 2021, **991**, 164963.
36 J. Hui, P. Ran, Y. Su, L. Yang, X. Xu, T. Liu and Y. M. Yang, High-Resolution X-ray Imaging Based on Solution-Phase-Synthesized $Cs_3Cu_2I_5$ Scintillator Nanowire Array, The, *J. Phys. Chem. C*, 2022, **126**(30), 12882–12888.
37 B. Wang, P. Li, Y. Zhou, Z. Deng, X. Ouyang and Q. Xu, $Cs_3Cu_2I_5$ Perovskite Nanoparticles in Polymer Matrix as Large-Area Scintillation Screen for High-Definition X-ray Imaging, *ACS Appl. Nano Mater.*, 2022, **5**(7), 9792–9798.
38 Q. Wang, Ce Wang, Z. Wang, X. Sun, M. Nikl, X. OuYang and Y. Wu, Achieving Efficient Neutron and Gamma Discrimination in a Highly Stable 6Li-Loaded Cs3Cu2I5 Perovskite Scintillator, *J. Phys. Chem. Lett.*, 2022, **13**(39), 9066–9071.
39 X. Liu, Y. Yu, F. Yuan, C. Zhao, H. Dong, B. Jiao and Z. Wu, Vacuum Dual-Source Thermal-Deposited Lead-Free Cs3Cu2I5 Films with High Photoluminescence Quantum Yield for Deep-Blue Light-Emitting Diodes, *ACS Appl. Mater. Interfaces*, 2020, **12**(47), 52967–52975.
40 S. Seth and A. Samanta, Photoluminescence of Zero-Dimensional Perovskites and Perovskite-Related Materials, *J. Phys. Chem. Lett.*, 2018, **9**(1), 176–183.
41 P. Cheng, L. Sun, L. Feng, S. Yang, Y. Yang, D. Zheng, Y. Zhao, Y. Sang, R. Zhang, D. Wei, W. Deng and K. Han, Colloidal Synthesis and Optical Properties of All-Inorganic Low-Dimensional Cesium Copper Halide Nanocrystals, *Angew. Chem., Int. Ed.*, 2019, **58**(45), 16087–16091.
42 R. Kentsch, M. Morgenroth, M. Scholz, K. Xu, J. Schmedt Auf der Gunne, T. Lenzer and K. Oum, Direct Observation of the Exciton Self-Trapping Process in CsCu2I3 Thin Films, *J. Phys. Chem. Lett.*, 2020, **11**(11), 4286–4291.
43 M. Nikl, Scintillation detectors for x-rays, *Meas. Sci. Technol.*, 2006, **17**(4), R37.
44 C. L. Wang, Particle Discrimination for Scintillator Neutron Detectors Using Graph Signal Processing, *IEEE Nuclear Science Symposium and Medical Imaging Conference*, 2022.
45 M. Zhang, X. Wang, B. Yang, J. Zhu, G. Niu, H. Wu, L. Yin, X. Du, M. Niu, Y. Ge, Q. Xie, Y. Yan and J. Tang, Metal Halide Scintillators with Fast and Self-Absorption-Free Defect-Bound Excitonic Radioluminescence for Dynamic X-Ray Imaging, *Adv. Funct. Mater.*, 2021, **31**(9), 2007921.
46 C. L. Wang, Gd-containing scintillators for thermal neutron detection *via* graph-based particle discrimination, *Rev. Sci. Instrum.*, 2021, **92**(10), 103304.
47 P. Yu, X. Wen, Y.-R. Toh and J. Tang, Temperature-Dependent Fluorescence in Carbon Dots, The, *J. Phys. Chem. C*, 2012, **116**(48), 25552–25557.
48 M. N. Nordin, J. Li, S. K. Clowes and R. J. Curry, Temperature dependent optical properties of PbS nanocrystals, *Nanotechnology*, 2012, **23**(27), 275701.
49 D. Valerini, A. Cretí, M. Lomascolo, L. Manna, R. Cingolani and M. Anni, Temperature dependence of the photoluminescence properties of colloidal CdS/ZnS core/shell quantum dots embedded in a polystyrene matrix, *Phys. Rev. B: Condens. Matter Mater. Phys.*, 2005, **71**(23), 235409.
50 C.-Y. Chen, Y.-I. Lin, P.-T. Lai, H.-C. Lin, G.-H. Tan, H.-W. Lin and R. D. Schaller, Self-Trapped and Free Exciton Dynamics in Vacuum-Deposited Cesium Copper Iodide Thin Films, *Adv. Opt. Mater.*, 2022, **10**(17), 2200005.
51 Z. Luo, Q. Li, L. Zhang, X. Wu, L. Tan, C. Zou, Y. Liu and Z. Quan, 0D $Cs_3Cu_2X_5$ (X = I, Br, and Cl) Nanocrystals: Colloidal Syntheses and Optical Properties, *Small*, 2020, **16**(3), 1905226.
52 R. Lin, Q. Zhu, Q. Guo, Y. Zhu, W. Zheng and F. Huang, Dual Self-Trapped Exciton Emission with Ultrahigh Photoluminescence Quantum Yield in $CsCu_2I_3$ and $Cs_3Cu_2I_5$ Perovskite Single Crystals, *J. Phys. Chem. C*, 2020, **124**(37), 20469–20476.

53 F. Gao, X. Zhu, Q. Feng, W. Zhong, W. Liu, H. Xu and Y. Liu, Deep-blue emissive $Cs_3Cu_2I_5$ perovskites nanocrystals with 96.6% quantum yield via InI3-assisted synthesis for light-emitting device and fluorescent ink applications, *Nano Energy*, 2022, **98**, 107270.

54 L.-T. Wang, Z.-Z. Ma, F. Zhang, M. Wang, X. Chen, D. Wu, Y.-T. Tian, X.-J. Li and Z.-F. Shi, Stable down-conversion white light-emitting devices based on highly luminescent copper halides synthesized at room temperature, *J. Mater. Chem. C*, 2021, **9**(19), 6151–6159.